Received: 23 May 2023 | Revised: 4 May 2024 | Accepted: 26 May 2024

DOI: 10.1002/qj.4787

Quarterly Journal of the Royal Meteorological Society RMetS

RESEARCH ARTICLE

An analytical model for daily-periodic slope winds. Part 2: Solutions

Mattia Marchio[1,2] | **Sofia Farina**[1,2] | **Dino Zardi**[1,2]

[1]Atmospheric Physics Group, Department of Civil, Environmental and Mechanical Engineering (DICAM), University of Trento, Trento, Italy

[2]Center Agriculture Food Environment (C3A), University of Trento, Trento, Italy

Correspondence
Mattia Marchio and Dino Zardi, Atmospheric Physics Group, Department of Civil, Environmental and Mechanical Engineering, University of Trento, Via Mesiano 77, Trento 38122, Italy.
Email: mattia.marchio@unitn.it
dino.zardi@unitn.it

Funding information
Italian Ministry for Universities and Research; European Union "NextGenerationEU" and Italian Ministry of University and Research, Prot.2022NEWP4J, CUPE53D23004450006

Abstract

This article presents an analytical model for the diurnal cycle of slope-normal profiles of potential temperature and wind speed characterizing thermally driven slope winds, generated by a daily-periodic surface energy budget. The model extends the solution proposed by Zardi and Serafin, originally formulated for a pure sinusoidal surface forcing temperature. To account for the asymmetric features characterizing the daytime and nighttime phases, a full Fourier series expansion is derived, the coefficients and phases of which are prescribed from the surface energy budget driven by the daily-periodic radiation model described in Part 1 of the present work. The model is applicable for any slope angle ($0° \leq \alpha \leq 90°$) and orientation, at any latitude and elevation (up to 2500 m), and for all seasons. Despite some inherent limitations, the most remarkable being the absence of moist processes and latent heat fluxes, the model captures most key features of daily-periodic slope wind systems, in particular the asymmetry between daytime and nighttime phases. Moreover, it allows exploration of the sensitivity of these flows to the various factors concurring in their development, and offers a basis for more realistic analytical solutions for slope winds.

KEYWORDS

analytical model, daily cycle, slope winds, surface energy budget, thermally driven circulations

1 | INTRODUCTION

Diurnal wind systems, generated by the cycle of daytime heating and nighttime cooling over sloping surfaces under clear-sky conditions, are very peculiar and ubiquitous features of mountainous terrains (e.g., Zardi & Whiteman, 2013). Despite their relevance for a variety of applications, ranging from pollutant transport to convection initiation, slope winds are far from being fully understood and their structure and development still pose many open questions for scientific investigations (e.g., De Wekker *et al.*, 2018, Serafin *et al.*, 2018). Clear skies allow significant amounts of incoming solar radiation during daytime and radiation loss during nighttime (Laiti *et al.*, 2014; Giovannini *et al.*, 2017). The resulting daily cycles of net radiation at the surface promote a series of buoyancy-driven flows over complex terrain, also named *thermally driven*. These consist of winds typically blowing up the slopes during the day and down the slopes during the night, separated by two transition phases around sunset and sunrise (Farina *et al.*, 2023). Slope winds also exhibit a strong seasonality, with summer months more prone to their development, as the incoming radiation is a controlling factor for their strength.

For simple slopes, an analytical solution for the slope-normal structure of wind and temperature perturbations was offered by the milestone work by Prandtl (1942). This solution has shown mixed success when compared with observations. In fact, Defant (1949) found that the analytical solution agrees fairly well with data from field measurements for the downslope component, while significant discrepancies are found for the upslope one. Various authors extended the Prandtl (1942) model taking into account additional factors, such as Coriolis force (Stiperski *et al.*, 2007), changing slope angle (Zammett & Fowler, 2007), and non-constant eddy viscosity (Grisogono & Oerlemans, 2001; Grisogono *et al.*, 2014). However, all these models provide solutions for steady forcing.

Time-dependent solutions were first proposed by Defant (1949) as an extension of Prandtl (1942). However, Zardi and Serafin (2015) showed that such solutions are an approximation of the full ones, which they derived in terms of a time-varying vertical structure of air temperature and along-slope wind speed in response to a sinusoidal surface temperature cycle. In particular, they found two different wind regimes, depending on the frequency of the surface forcing ω, the slope angle α, and the intrinsic buoyancy frequency of the unperturbed atmosphere N: a *supercritical* regime occurs for $\omega < N \sin\alpha$, while a *subcritical* one occurs in the opposite situation. Given the sinusoidal nature of the surface forcing and the constant eddy coefficients, the resulting wind and temperature profiles exhibit fully symmetric responses for daytime and nighttime phases. However, field observations show remarkable differences between the two regimes in terms of both magnitude and height of the peak of wind velocity, as well as different timings for nighttime and daytime and for the two reversal phases (e.g., Whiteman, 2000; Farina & Zardi, 2023). This suggests that a more realistic surface forcing should be taken into account to explain the daytime/nighttime differences. In particular, topographical factors, playing a major role in determining the radiation reaching the surface, need to be taken properly into account for a realistic analysis (Castelli *et al.*, 2014; Laiti *et al.*, 2018).

Accordingly, in the present work, time-dependent analytical solutions are derived, based on a surface energy budget (SEB) accounting for the partitioning of the net radiation available at the surface into sensible and ground heat fluxes. The latter are obtained through a daily-periodic analytical function describing the daily cycle of incoming solar radiation introduced in Part 1 of the present work. Hence, the sinusoidal surface forcing of Zardi and Serafin (2015) is extended into a full Fourier series expansion including higher-order harmonics, the amplitudes and phases of which are determined from the SEB.

The article is organized as follows. Section 2 presents the formulation of the problem, summarizes the analytical solutions available in the literature (for both stationary and time-dependent cases), and finally presents the extended analytical solutions, along with the formulation of the boundary conditions from the SEB. Section 3 shows the results of the new solutions in different conditions, that is, different days of the year, different slope angles, and orientations, with a focus on the role of the different harmonics and on some case limits. Finally, Section 4 presents the discussion, including the limitations of the model, and conclusions.

2 | FORMULATION OF THE PROBLEM AND NEW SOLUTIONS

2.1 | Governing equations and existing solutions

Let us consider an ideal slope, that is, an infinitely extended tilted plane, with a slope angle α. As customary, we adopt a rotated Cartesian frame of reference (Figure 1), with s the along-slope coordinate and n the slope-normal one (the spanwise coordinate is not needed, as the process is essentially two-dimensional (2-D)). A vertical axis with coordinate $z = s\sin\alpha + n\cos\alpha$ is also retained for convenience. The ambient atmosphere is stably stratified, with a reference surface value of potential temperature θ_{00} at the reference height $z = 0$ and a constant vertical gradient γ_a for the potential temperature, such that the unperturbed ambient atmosphere exhibits the following thermal structure:

$$\theta_0 = \theta_{00} + \gamma_a\, z = \theta_{00} + \gamma_a\,(s\sin\alpha + n\cos\alpha). \qquad (1)$$

The daily cycle of daytime surface heating and nighttime cooling produces a perturbation θ of the potential temperature, which can be split, like the other variables, namely the along-slope u and slope-normal w wind velocity components, into a mean and a fluctuating part, according to Reynolds decomposition:

$$\theta = \overline{\theta} + \theta', \qquad w = \overline{w} + w', \qquad u = \overline{u} + u'. \qquad (2)$$

Reynolds-averaged Navier–Stokes equations are then obtained from the momentum and energy equations, assuming the Boussinesq approximation and neglecting the slope-normal mean velocity, as well as the Coriolis force. Assuming the flow is invariant along the slope, all quantities will depend only on the slope-normal coordinate and on time. Hence, the governing equations are

$$\frac{\partial\overline{u}}{\partial t} = \overline{\theta}\frac{N^2}{\gamma_a}\sin\alpha - \frac{\partial}{\partial n}\overline{u'w'}, \qquad (3)$$

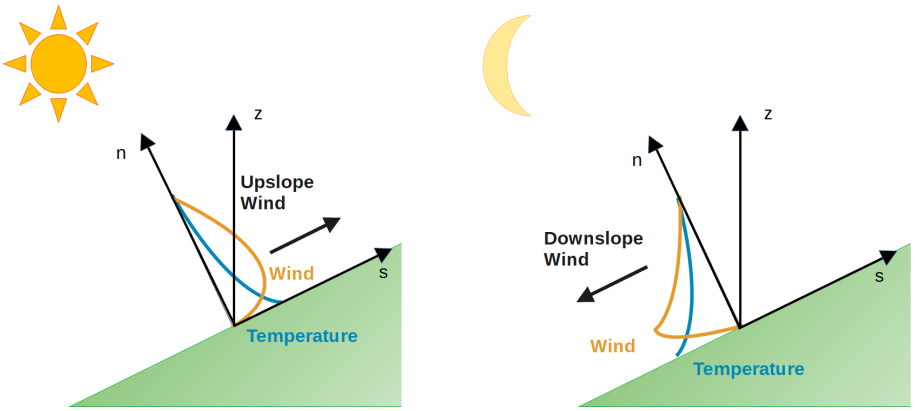

FIGURE 1 Schematics of daytime upslope winds (left panel) and nighttime downslope winds (right panel). Adapted from Barry (2008), Hatchett *et al.* (2020), and Whiteman (2000).

$$\frac{\partial \overline{\theta}}{\partial t} = -\overline{u}\gamma_a \sin\alpha - \frac{\partial}{\partial n}\overline{w'\theta'}, \tag{4}$$

where $N = (\gamma_a\, g/\theta_{00})^{1/2}$ is the buoyancy frequency of the unperturbed atmosphere, g is the acceleration due to gravity, and t the time. For convenience, hereinafter we assume $t = 0$ at solar noon.

Applying a first-order closure for turbulent heat $\overline{w'\theta'}$ and momentum $\overline{u'w'}$ fluxes:

$$\overline{u'w'} = -K_m \frac{\partial \overline{u}}{\partial n}, \qquad \overline{w'\theta'} = -K_h \frac{\partial \overline{\theta}}{\partial n}, \tag{5}$$

with constant eddy viscosity K_m and eddy diffusivity K_h, Equations (3) and (4) can be rewritten as

$$\frac{\partial \overline{u}}{\partial t} = \overline{\theta}\frac{N^2}{\gamma_a}\sin\alpha + K_m \frac{\partial^2 \overline{u}}{\partial n^2}, \tag{6}$$

$$\frac{\partial \overline{\theta}}{\partial t} = -\overline{u}\gamma_a \sin\alpha + K_h \frac{\partial^2 \overline{\theta}}{\partial n^2}. \tag{7}$$

Notice that this is a set of linear partial differential equations with constant coefficients. Daily periodic solutions can easily be found by superpositions of harmonic components through a Fourier series expansion.

2.1.1 | Steady-state solutions (Prandtl, 1942)

The steady-state analytical solution of Equations (6) and (7) provided by Prandtl (1942) represents either an upslope or downslope steady flow regime, as a response to a constant surface-temperature perturbation ΔT_s, assuming a no-slip boundary condition at the surface and vanishing perturbations away from the surface:

$$\overline{u}(n) = U e^{-n/l}\sin(n/l), \tag{8}$$

$$\overline{\theta}(n) = \Delta T_s e^{-n/l}\cos(n/l), \tag{9}$$

where $Pr_t = K_m/K_h$ is the turbulent Prandtl number, which will hereinafter be assumed equal to one ($K_m = K_h = K$), and l is a length-scale defined as

$$l = \left(\frac{2K}{N\sin\alpha}\right)^{1/2}, \tag{10}$$

whereas the velocity scale U is

$$U = \Delta T_s \frac{N}{\gamma_a} Pr_t^{-1/2}. \tag{11}$$

Notice that a positive potential temperature anomaly $\Delta T_s > 0$ is associated with an upslope flow ($U > 0$), whereas a negative one produces a downslope flow.

2.1.2 | Time-dependent solutions (Zardi & Serafin, 2015)

Zardi and Serafin (2015) assumed a sinusoidal surface temperature forcing:

$$\overline{\theta}(0,t) = \Delta T_s \sin(\omega t + \psi), \tag{12}$$

where $\omega = 7.272 \times 10^{-5}$ s^{-1} is the angular frequency associated with the daily period, and then identified two length scales:

$$l_+ = \left(\frac{2K}{\omega_+}\right)^{1/2}, \qquad l_- = \left(\frac{2K}{\omega_-}\right)^{1/2}, \tag{13}$$

where

$$\omega_+ = N\sin\alpha + \omega, \qquad \omega_- = N\sin\alpha - \omega. \tag{14}$$

They found two different sets of solutions, depending on the flow regime, which is determined by the value of $N\sin\alpha$, compared with the frequency of the surface forcing.

In the *supercritical regime* ($N\sin\alpha > \omega$), corresponding to steep slopes or strong stability, the solutions are

$$\overline{u} = \frac{\Delta T_s}{2}\frac{N}{\gamma_a}\left[e^{-n/l_+}\cos\left(\omega t - \frac{n}{l_+} + \psi\right) - e^{-n/l_-}\cos\left(\omega t + \frac{n}{l_-} + \psi\right)\right], \quad (15)$$

$$\overline{\theta} = \frac{\Delta T_s}{2}\left[e^{-n/l_+}\sin\left(\omega t - \frac{n}{l_+} + \psi\right) + e^{-n/l_-}\sin\left(\omega t + \frac{n}{l_-} + \psi\right)\right]. \quad (16)$$

Here the solution exhibits a strong coupling between near-surface and upper levels. Flow reversal from upslope to downslope and vice versa occurs in phase at all levels.

In the *subcritical regime* ($N\sin\alpha < \omega$), that is, gentle slopes or weak stability, the solutions are

$$\overline{u} = \frac{\Delta T_s}{2}\frac{N}{\gamma_a}\left[e^{-n/l_+}\cos\left(\omega t - \frac{n}{l_+} + \psi\right) - e^{-n/|l_-|}\cos\left(\omega t - \frac{n}{|l_-|} + \psi\right)\right], \quad (17)$$

$$\overline{\theta} = \frac{\Delta T_s}{2}\left[e^{-n/l_+}\sin\left(\omega t - \frac{n}{l_+} + \psi\right) + e^{-n/|l_-|}\sin\left(\omega t - \frac{n}{|l_-|} + \psi\right)\right]. \quad (18)$$

Here a significant phase lag characterizes the response at higher levels with respect to the reaction of the system to surface forcing in the near-surface levels, that is, the coupling between the layers is rather weak.

A third flow regime, named *critical* ($N\sin\alpha = \omega$), occurs when the buoyancy frequency and the forcing frequency exactly match their values. However this is quite unlikely to occur in real situations and will not be considered here.

2.2 | Extended solutions

The surface temperature forcing proposed by Zardi and Serafin (2015) is purely sinusoidal, thus implying symmetric daytime and nighttime regimes. However, observations suggest that daytime upslope flows exhibit stronger peak velocities at higher levels above the ground than the nighttime regime (e.g., Mahrt & Larsen, 1990; Whiteman, 2000).

We indicate the surface temperature at any time t as

$$T(0,t) = \overline{T} + \Delta T, \quad (19)$$

where $\overline{T}$ is the mean annual temperature and $\Delta T = \Delta T_d + \Delta T_s$, with ΔT_d being the difference between the mean daily temperature of a single day and the annual mean, and ΔT_s being the amplitude of the daily cycle around the daily mean temperature. This amplitude can be expressed as a Fourier series expansion:

$$\Delta T_s = \sum_{m=1}^{\infty}\Delta T_{sm}\sin(m\omega t + \psi_m), \quad (20)$$

where ΔT_{sm} and ψ_m are amplitudes and phases. The values of the parameters $\overline{T}$, ΔT_d, ΔT_{sm}, and ψ_m will be obtained below, from the SEB. Solutions of Equations (6) and (7) can be sought in terms of a combination of expressions like Equations (15)–(16) or (17)–(18), depending on the values of the length scales. In particular, for each harmonic a pair of length scales can be obtained:

$$l_{m+} = \left(\frac{2K}{\omega_{m+}}\right)^{1/2}, \qquad l_{m-} = \left(\frac{2K}{\omega_{m-}}\right)^{1/2}, \quad (21)$$

with

$$\omega_{m+} = N\sin\alpha + m\omega, \qquad \omega_{m-} = N\sin\alpha - m\omega. \quad (22)$$

Remarkably, the flow regime (subcritical or supercritical) for the mth harmonic is determined by the value of $m\omega$ with respect to $N\sin\alpha$. This is of particular importance for the case in which at least the first harmonic satisfies the condition for the supercritical regime ($N\sin\alpha > \omega$). In fact, higher order harmonics ($2\omega, 3\omega, ..$) may instead be subcritical. Assuming that the first harmonic represents the fundamental flow regime, one can rewrite Equation (19) to provide time-dependent vertical profiles of potential temperature for the two flow regimes. The new solutions for potential temperature and wind speed are as follows.

- *Supercritical regime*: $N\sin\alpha > \omega$:

$$\theta(t,n) = \overline{T} + \gamma_a\sin\alpha n + \Delta T_d e^{-n/l}\cos(n/l) + \sum_{m=1}^{m_c}\frac{\Delta T_{sm}}{2}\left[e^{-n/l_{m+}}\sin\left(m\omega t - \frac{n}{l_{m+}} + \psi_m\right) + e^{-n/l_{m-}}\sin\left(m\omega t + \frac{n}{l_{m-}} + \psi_m\right)\right] + \sum_{m=m_c+1}^{\infty}\frac{\Delta T_{sm}}{2}\left[e^{-n/l_{m+}}\sin\left(m\omega t - \frac{n}{l_{m+}} + \psi_m\right) + e^{-n/|l_{m-}|}\sin\left(m\omega t - \frac{n}{|l_{m-}|} + \psi_m\right)\right], \quad (23)$$

$$u(t,n) = \Delta T_d\frac{N}{\gamma_a}e^{-n/l}\sin(n/l) + \sum_{m=1}^{m_c}\frac{\Delta T_{sm}}{2}\frac{N}{\gamma_a}\left[e^{-n/l_{m+}}\cos\left(m\omega t - \frac{n}{l_{m+}} + \psi_m\right)\right.$$

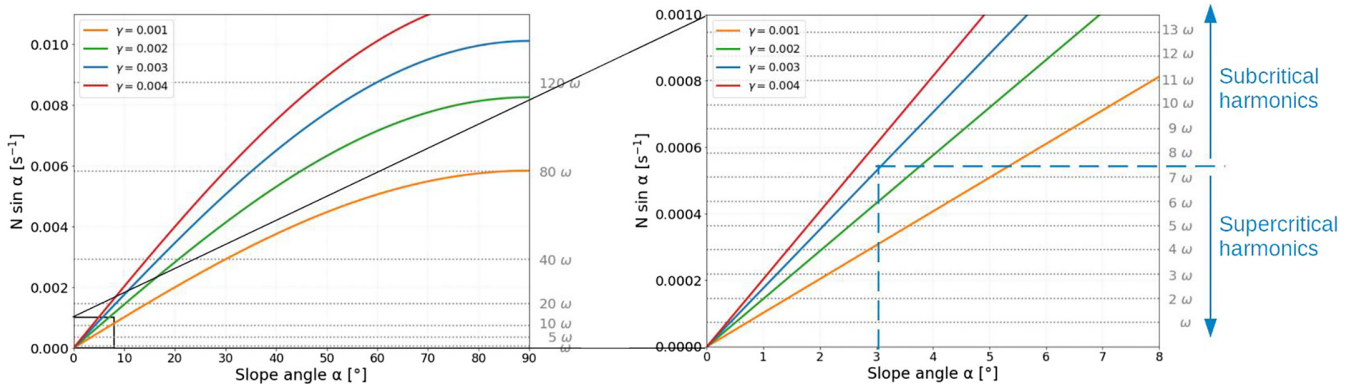

FIGURE 2 Values of $N \sin \alpha$ as a function of the slope angle α for different values of γ_a. The chart allows determination of which harmonics fall in the supercritical regime conditions and which are instead subcritical for a given slope angle. The example in blue considers a background atmosphere with $\gamma_a = 0.003\ \mathrm{K \cdot m^{-1}}$ and $\alpha = 3°$. Here $7\omega < N \sin\alpha < 8\omega$, hence $m_c = 7$.

$$-e^{-n/l_{m-}} \cos\left(m\omega t + \frac{n}{l_{m-}} + \psi_m\right)\Bigg] + \sum_{m=m_c+1}^{\infty} \frac{\Delta T_{sm}}{2} \frac{N}{\gamma_a}\left[e^{-n/l_{m+}} \cos\left(m\omega t - \frac{n}{l_{m+}} + \psi_m\right) - e^{-n/|l_{m-}|} \cos\left(m\omega t - \frac{n}{|l_{m-}|} + \psi_m\right)\right], \quad (24)$$

where m_c indicates the threshold harmonic, with harmonics of order higher than m_c becoming subcritical, that is, $N \sin\alpha > \omega_m$ for $m > m_c$. Figure 2 shows which harmonics fall either in the supercritical or subcritical regimes according to the slope angle and the atmospheric stability (γ_a).

- *Subcritical regime*: $N \sin\alpha < \omega$:

$$\theta(t,n) = \overline{T} + \gamma_a \cos\alpha n + \Delta T_d e^{-n/l} \cos(n/l) + \sum_{m=1}^{\infty} \frac{\Delta T_{sm}}{2}\left[e^{-n/l_{m+}} \sin\left(m\omega t - \frac{n}{l_{m+}} + \psi_m\right) + e^{-n/|l_{m-}|} \sin\left(m\omega t - \frac{n}{|l_{m-}|} + \psi_m\right)\right], \quad (25)$$

$$u(t,n) = \Delta T_d \frac{N}{\gamma_a} e^{-n/l} \sin(n/l) + \sum_{m=1}^{\infty} \frac{\Delta T_{sm}}{2} \frac{N}{\gamma_a}\left[e^{-n/l_{m+}} \cos\left(m\omega t - \frac{n}{l_{m+}} + \psi_m\right) - e^{-n/|l_{m-}|} \cos\left(m\omega t - \frac{n}{|l_{m-}|} + \psi_m\right)\right]. \quad (26)$$

In this case, there is no need for a threshold harmonic, as all of them are individually subcritical. If the first harmonic fulfills the subcritical condition ($\omega > N \sin\alpha$), then all the higher-order ones do so.

2.3 | Solution of the SEB

The coefficients defining the solution are derived from the SEB, which in the most general terms can be written as

$$R_{net} = H + G + LE + S, \quad (27)$$

where H is the sensible heat flux, G the ground heat flux, LE the latent heat flux, and S the storage. Here we will assume that the only contribution to the sensible heat flux is given by the thermally driven slope winds, that is, we will neglect any other heat transport process, such as convection or large-scale transport. As we are interested here in simple surfaces (i.e., no roughness or canopy layer) and dry processes, we will neglect the storage S, as well as the latent heat flux LE. Accordingly, substituting from Equation (5), Equation (27) can be expressed as a function of air (θ) and ground (T_g) temperatures:

$$R_{net} = H + G = -\rho\ c_{pd}\ K\ \frac{\partial\theta}{\partial n}\Big|_{n=0} + \rho_g\ c_{pg}\ K_g\ \frac{\partial T_g}{\partial n}\Big|_{n=0}, \quad (28)$$

where ρ is the air density, c_{pd} the specific heat at constant pressure of dry air, ρ_g the density of the soil, c_{pg} the specific heat of the soil, K_g the heat diffusivity of the soil, and T_g the ground temperature. The temperature structure in the ground is governed by the heat conduction equation,

$$\frac{\partial T_g}{\partial t} = K_g \frac{\partial^2 T_g}{\partial n^2}. \quad (29)$$

The surface ($n = 0$) value of T_g needs to match the surface atmospheric temperature given by Equation (19). This requirement imposes one further condition on the temperature gradient in the soil, which must be equal to the one for the unperturbed atmosphere. According to Carslaw

and Jaeger (1959), the expression for T_g then assumes the structure

$$T_g(n,t) = T_{g0} - \gamma_a \cos\alpha n + \sum_{m=1}^{\infty} \Delta T_{sm} \sin\left(m\omega t + \frac{n}{l_{gm}} + \psi_m\right) e^{n/l_{gm}}, \quad (30)$$

where T_{g0} is the reference surface temperature:

$$T_{g0} = \overline{T} + \Delta T_d, \quad (31)$$

and l_{gm} is a characteristic length scale:

$$l_{gm} = \left(\frac{2K_g}{m\omega}\right)^{1/2}. \quad (32)$$

Substituting Equation (30) in Equation (28), for the supercritical case, we get

$$\begin{aligned} H + G &= \rho\, c_{pd}\, K\left(-\gamma_a \cos\alpha + \frac{\Delta T_d}{l}\right) - \rho_g\, c_{pg}\, K_g\, \gamma_a \cos\alpha \\ &+ \sum_{m=1}^{m_c} \Delta T_{sm} \left[\left(\rho\, c_{pd}\left(\frac{K}{2l_{m+}} + \frac{K}{2l_{m-}}\right) + \rho_g\, c_{pg}\, \frac{K_g}{l_{gm}}\right) \right. \\ &\times \sin(m\omega t + \psi_m) + \left\{\rho\, c_{pd}\left(\frac{K}{2l_{m+}} - \frac{K}{2l_{m-}}\right)\right. \\ &\left.\left. + \rho_g\, c_{pg}\, \frac{K_g}{l_{gm}}\right\} \cos(m\omega t + \psi_m)\right] \\ &+ \sum_{m=m_c+1}^{\infty} \Delta T_{sm} \left[\left\{\rho\, c_{pd}\left(\frac{K}{2l_{m+}} + \frac{K}{2|l_{m-}|}\right)\right.\right. \\ &\left. + \rho_g\, c_{pg}\, \frac{K_g}{l_{gm}}\right\} \sin(m\omega t + \psi_m) \\ &+ \left(\rho\, c_{pd}\left(\frac{K}{2l_{m+}} + \frac{K}{2|l_{m-}|}\right)\right. \\ &\left.\left. + \rho_g\, c_{pg}\, \frac{K_g}{l_{gm}}\right) \cos(m\omega t + \psi_m)\right]. \end{aligned} \quad (33)$$

For the subcritical case, we would get an identical expression, with the exception that, since the first harmonic is subcritical, all harmonics fall in the subcritical flow regime (i.e. $m_c = 0$).

To derive $\overline{T}$, ΔT_d, ΔT_{sm}, and ψ_m from Equation (33), the left-hand side (l.h.s.) of the SEB Equation (28) needs to be expanded into a Fourier series as well.

An expression for net surface radiation was presented in Part 1 of the present work (Marchio *et al.*, 2024):

$$R_{net}(t) = K_{net} + L_{net} = (1-A)K^*_{0_T} + (1-A) \times \sum_{m=1}^{\infty} K^*_m \sin(m\omega t + \xi_m) + \epsilon_s \epsilon_a \sigma T_a^4 - \epsilon_s \sigma T_s^4, \quad (34)$$

where $K^*_{0_T}$ is the daily mean value of net radiation, K^*_m and ξ_m the amplitude and phase of the harmonics of the incoming shortwave radiation, A the surface albedo, ϵ_a and ϵ_s the atmosphere and surface emissivities respectively, $\sigma = 5.67 \times 10^{-8}\,\mathrm{W{\cdot}m^{-2}\cdot K^{-4}}$ the Stefan–Boltzmann constant, T_a the average atmospheric temperature, and T_s the surface temperature. Here we will assume that T_a is conveniently represented by the screen-level temperature, that is, the temperature at 2 m AGL (h_r).

Introducing the linearization

$$T_s^4 = \overline{T}^4 \left(1 + \frac{\Delta T}{\overline{T}}\right)^4 \approx \overline{T}^4 \left(1 + 4\frac{\Delta T}{\overline{T}}\right), \quad (35)$$

we get

$$L_{out} = -\epsilon_s \sigma T_s^4 \approx -\epsilon_s \sigma \overline{T}^4 - 4\epsilon_s \sigma \overline{T}^3 \Delta T_d - 4\epsilon_s \sigma \overline{T}^3 \sum_{m=1}^{\infty} \Delta T_{sm} \sin(m\omega t + \psi_m). \quad (36)$$

The same linearization is performed on the incoming longwave radiation. To assess the applicability of the above linearizations, we computed the relative error introduced in the net longwave radiation for a range of plausible mean annual radiative temperatures, considering the largest possible seasonal and daily anomalies ($\Delta T_D = 15\,\mathrm{K}$ and $\Delta T_s = 10\,\mathrm{K}$). The relative error was found to remain under 6%, thus justifying the use of linearization for the purposes of the present work.

Equation (34) can thus be rewritten as

$$\begin{aligned} R_{net} &= (1-A)K^*_{0_T} + \epsilon_s \epsilon_a \sigma \overline{T}^4 \\ &+ 4\epsilon_s \epsilon_a \sigma \overline{T}^3 \Delta T_d e^{-h_r/l} \cos\left(\frac{h_r}{l}\right) \\ &- \epsilon_s \sigma \overline{T}^4 - 4\epsilon_s \sigma \overline{T}^3 \Delta T_d \\ &+ (1-A) \sum_{m=1}^{\infty} \left[K^*_m \sin(m\omega t + \xi_m)\right] \\ &+ 4\epsilon_s \epsilon_a \sigma \overline{T}^3 \sum_{m=1}^{m_c} \frac{\Delta T_{sm}}{2} \\ &\times \left[e^{-h_r/l_{m+}} \left(\cos\left(-\frac{h_r}{l_{m+}}\right) \sin(m\omega t + \psi_m) \right.\right. \\ &\left. - \sin\left(\frac{h_r}{l_{m+}}\right) \cos(m\omega t + \psi_m)\right) \\ &+ e^{-h_r/l_{m-}} \left(\cos\left(\frac{h_r}{l_{m-}}\right) \sin(m\omega t + \psi_m)\right. \\ &\left.\left. + \sin\left(\frac{h_r}{l_{m-}}\right) \cos(m\omega t + \psi_m)\right)\right] \end{aligned}$$

$$+ 4\epsilon_s\epsilon_a\sigma \sum_{m=m_c+1}^{\infty} \frac{\Delta T_{sm}}{2}$$
$$\times \left[e^{-h_r/l_{m+}} \left(\cos\left(-\frac{h_r}{l_{m+}} \right) \sin(m\omega t + \psi_m) \right.\right.$$
$$\left. - \sin\left(\frac{h_r}{l_{m+}} \right) \cos(m\omega t + \psi_m) \right) + e^{-h_r/|l_{m-}|}$$
$$\times \left(\cos\left(-\frac{h_r}{|l_{m-}|} \right) \sin(m\omega t + \psi_m) \right.$$
$$\left.\left. -\sin\left(\frac{h_r}{|l_{m-}|} \right) \cos(m\omega t + \psi_m) \right) \right]$$
$$- 4\epsilon_s\sigma\overline{T}^3 \sum_{m=1}^{\infty} \Delta T_{sm} \sin(m\omega t + \psi_m). \quad (37)$$

Substituting Equation (33) into the right-hand side (r.h.s.) of Equation (28), and Equation (37) into the l.h.s., one finally gets suitable conditions for determining the reference parameters $\overline{T}$, ΔT_d, ΔT_{sm}, and ψ_m.

In particular, taking the annual mean of both sides, one obtains

$$(1-A)\overline{K^*_{0_T}} + \epsilon_s\epsilon_a\sigma\overline{T}^4 - \epsilon_s\sigma\overline{T}^4 = -\rho\, c_{pd}\, K\gamma_a \cos\alpha - \rho_g\, c_{pg}\, K_g\, \gamma_a \cos\alpha, \quad (38)$$

from which we can derive the formulation for $\overline{T}$:

$$\overline{T} = \left(\frac{(1-A)\overline{K^*_{0_T}} + (\rho\, c_{pd}\, K + \rho_g\, c_{pg}\, K_g)\, \gamma_a \cos\alpha}{(1-\epsilon_a)\, \epsilon_s\, \sigma} \right)^{1/4}. \quad (39)$$

The mean temperature provided by Equation (39) is actually a mean radiative temperature, that is, the temperature required to guarantee radiative equilibrium over the year. For this reason, it might be different from the mean temperature observed at a location. Notice that suitable adjustments can be made to parameterize the contributions from large-scale transport or convection, which are admittedly neglected here. Moreover, latent heat flux and the effect of clouds should be taken into account for more realistic outcomes.

The difference between the mean daily temperature and the mean annual temperature has to account for the radiative surplus or deficit on a single day with respect to the annual mean at the same point. Considering the daily mean of the SEB, we obtain

$$(1-A)\left(K^*_{0_T}\right) + \epsilon_s\epsilon_a\sigma\overline{T}^4 + 4\epsilon_s\epsilon_a\sigma\overline{T}^3\Delta T_d e^{-h_r/l}\cos\left(\frac{h_r}{l}\right) - \epsilon_s\sigma\overline{T}^4 - 4\epsilon_s\sigma\overline{T}^3\Delta T_d = \rho\, c_p\, K\left(-\gamma_a\cos\alpha + \frac{\Delta T_d}{l}\right) - \rho_g\, c_{pg}\, K_g\gamma_a\cos\alpha. \quad (40)$$

Hence, ΔT_d is given by

$$\Delta T_d = \frac{(1-A)\left(K^*_{0_T}\right) + \epsilon_s\epsilon_a\sigma\overline{T}^4 - \epsilon_s\sigma\overline{T}^4 + (\rho\, c_p\, K + \rho_g\, c_{pg}\, K_g)\gamma_a\cos\alpha}{-4\epsilon_s\epsilon_a\sigma\overline{T}^3 e^{-h_r/l}\cos\left(\frac{h_r}{l}\right) + 4\epsilon_s\sigma\overline{T}^3 + \frac{\rho\, c_p\, K}{l}}. \quad (41)$$

Finally, collecting likewise time-dependent terms and rearranging, we get

$$(1-A)\sum_{m=1}^{\infty} K^*_m \sin(m\omega t + \xi_m) = \sum_{m=1}^{m_c} \Delta T_{sm}\sqrt{a^2_{m_{SUP}} + b^2_{m_{SUP}}} \sin(m\omega t + \phi_{m_{SUP}} + \psi_m) + \sum_{m=m_c+1}^{\infty} \Delta T_{sm}\sqrt{a^2_{m_{SUB}} + b^2_{m_{SUB}}} \sin(m\omega t + \phi_{m_{SUB}} + \psi_m), \quad (42)$$

where

$$a_{m_{SUP}} = -2\epsilon_s\epsilon_a\sigma\,\overline{T}^3\left[e^{-h_r/l_{m+}}\cos\left(-\frac{h_r}{l_{m+}}\right) + e^{-h_r/l_{m-}}\cos\left(\frac{h_r}{l_{m-}}\right)\right] + 4\epsilon_s\sigma\overline{T}^3 + \rho\, c_{pd}\, K\left(\frac{1}{2l_{m+}} + \frac{1}{2l_{m-}}\right) + \rho_g\, c_{pg}\, K_g\, \frac{1}{l_{mg}},$$
$$b_{m_{SUP}} = -2\epsilon_s\epsilon_a\sigma\,\overline{T}^3\left[e^{-h_r/l_{m+}}\sin\left(-\frac{h_r}{l_{m+}}\right) + e^{-h_r/l_{m-}}\sin\left(\frac{h_r}{l_{m-}}\right)\right] + \rho\, c_{pd}\, K\left(\frac{1}{2l_{m+}} - \frac{1}{2l_{m-}}\right) + \rho_g\, c_{pg}\, K_g\, \frac{1}{l_{mg}}, \quad (43)$$

$$a_{m_{SUB}} = -2\epsilon_s\epsilon_a\sigma\,\overline{T}^3\left[e^{-h_r/l_{m+}}\cos\left(\frac{-h_r}{l_{m+}}\right) + e^{-h_r/|l_{m-}|}\cos\left(\frac{-h_r}{|l_{m-}|}\right)\right] + 4\epsilon_s\sigma\overline{T}^3 + \rho\, c_{pd}\, K\left(\frac{1}{2l_{m+}} + \frac{1}{2|l_{m-}|}\right) + \rho_g\, c_{pg}\, K_g\, \frac{1}{l_{mg}},$$
$$b_{m_{SUB}} = -2\epsilon_s\epsilon_a\sigma\overline{T}^3\left[e^{-h_r/l_{m+}}\sin\left(-\frac{h_r}{l_{m+}}\right) + e^{-h_r/|l_{m-}|}\sin\left(-\frac{h_r}{|l_{m-}|}\right)\right] + \rho\, c_{pd}\, K\left(\frac{1}{2l_{m+}} + \frac{1}{2|l_{m-}|}\right) + \rho_g\, c_{pg}\, K_g\, \frac{1}{l_{mg}}, \quad (44)$$

TABLE 1 Average values adopted for the examples of the present work, with the respective source indicated.

Variable	Symbol	Value	Source
Soil specific heat	c_{pg}	$837\,J\cdot K^{-1}\cdot kg^{-1}$	Carslaw and Jaeger (1959)
Soil density	ρ_g	$2500\,kg\cdot m^{-3}$	Carslaw and Jaeger (1959)
Soil heat diffusivity	K_g	$4.6\times10^{-7}\,m^2\cdot s^{-1}$	Carslaw and Jaeger (1959)
Air density	ρ	$1.225\,kg\cdot m^{-3}$	Carslaw and Jaeger (1959)
Air specific heat	c_p	$1004\,J\cdot K^{-1}\cdot kg^{-1}$	Carslaw and Jaeger (1959)
Air heat diffusivity	K	$1\,m^2\cdot s^{-1}$	Zardi and Serafin (2015)
Soil emissivity	ϵ_s	0.97	Van Wijk and Scholte Ubing (1963), An *et al.* (2017)
Clear-sky atm. emissivity	ϵ_a	0.72	Maykut and Church (1973)
Albedo	A	0.2	see Part 1

and

$$\phi_{m_{SUP}} = \arcsin\left(\frac{b_{m_{SUP}}}{\sqrt{a^2_{m_{SUP}} + b^2_{m_{SUP}}}}\right),$$
$$\phi_{m_{SUB}} = \arcsin\left(\frac{b_{m_{SUB}}}{\sqrt{a^2_{m_{SUB}} + b^2_{m_{SUP}}}}\right). \quad (45)$$

The amplitudes and phases of single harmonics can now be derived. For example, for a supercritical harmonic, we have

$$\Delta T_{sm} = \frac{(1-A)K^*_m}{\sqrt{a^2_{m_{SUP}} + b^2_{m_{SUP}}}} \quad (46)$$

and, finally,

$$\psi_m = \xi_m - \phi_{m_{SUP}}. \quad (47)$$

Similar expressions can be obtained for a subcritical harmonic simply by substituting $a_{m_{SUP}}$, $b_{m_{SUP}}$, and $\phi_{m_{SUP}}$ by $a_{m_{SUB}}$, $b_{m_{SUB}}$, and $\phi_{m_{SUB}}$, respectively.

3 | RESULTS

In this section we present results from the application of the model introduced above for a series of possible configurations, to explore their sensitivity to slope angle, slope orientation, and day of the year. Suitable representative values for the parameters adopted for the following examples are reported in Table 1.

In Part 1 of the present work it was shown that four harmonics are sufficient to describe the daily cycle of incoming radiation adequately. Hence, we will include four harmonics in the solutions represented below. Figure 3 supports this assumption, as it shows that amplitudes of harmonics higher than second-order are much smaller than the first two. It may be noted that, for steep ($\alpha > 30°$) south-facing slopes, the coefficients exhibit a local midsummer minimum. This is indeed a peculiarity of south-facing slopes: in summertime, when the sun is high above the horizon, the slope receives less radiation, due to both the higher inclination and the unfavorable orientation: their combination may result in the slope being less exposed to direct sunlight, thus reducing the amount of radiation reaching the surface.

3.1 | Mean annual radiative equilibrium temperature

Equation (40) provides the mean annual temperature $\overline{T}$ from radiative equilibrium, as a function of the annual mean of the constant term $(1-A)\overline{K^*_{0_T}}$. This term intrinsically accounts for local topographic factors such as slope angle and orientation.

Figure 4 shows the mean annual radiative equilibrium temperatures for different slope angles and orientations and latitudes, resulting from pointwise mean annual radiative equilibrium balance. These temperatures do not affect thermally driven slope winds, as they are mostly determined by the daily perturbation of surface temperature around the mean.

3.2 | Seasonal temperature anomalies and daily cycles of slope winds

The difference between the mean temperature of a given day and the mean annual radiative equilibrium temperature is determined by the surplus/deficit of daily radiation compared with the annual mean. This difference supports a steady-state Prandtl-like part of the solutions,

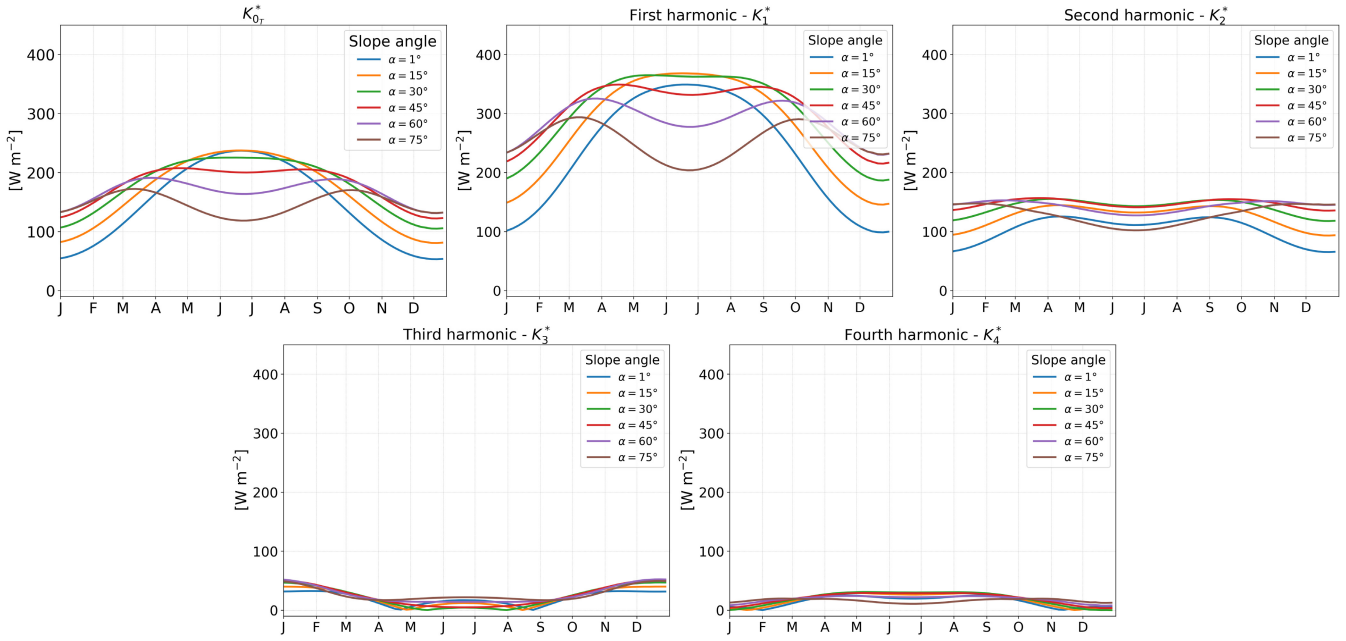

FIGURE 3 Values of the coefficient of the net radiation model from Part 1 as a function of the day of the year for a set of slope angles α, midlatitude ($\phi = 45°$), south-facing slope ($\gamma = 0°$, γ being the slope orientation angle).

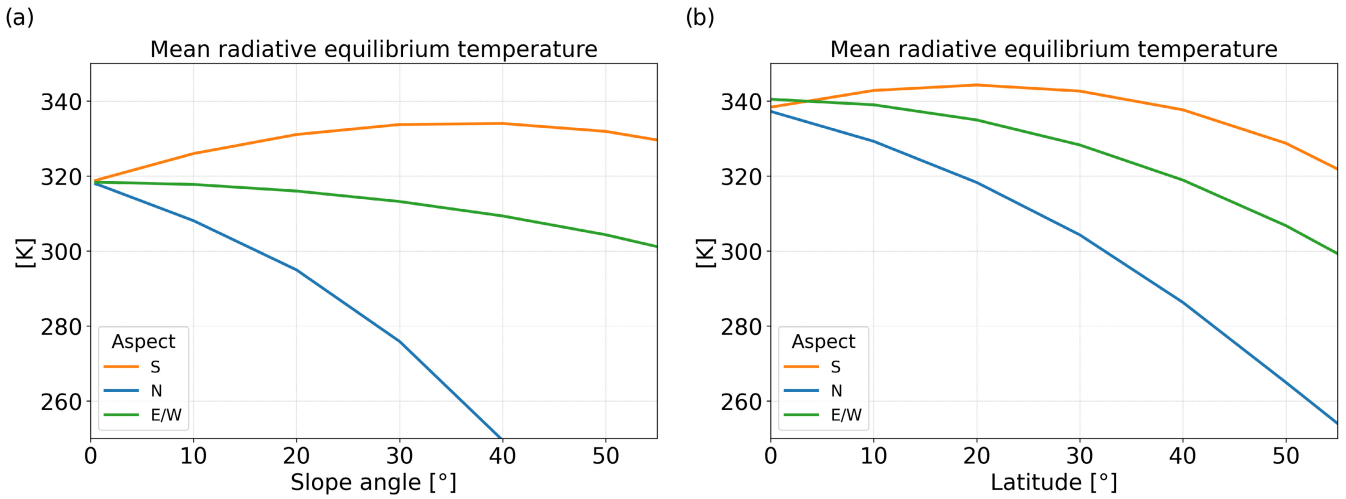

FIGURE 4 Mean annual radiative equilibrium temperature $\overline{T}$ for various slope orientations as a function of (a) slope angle, for fixed latitude $\phi = 45$o, and (b) latitude, for fixed slope angle $\alpha = 30$o.

either upslope or downslope according to the sign of this difference. Such a steady flow can be thought as a background flow enhancing or contrasting the development of daily-periodic slope winds. The seasonal temperature anomaly was computed for the south-facing slopes of Figure 4, as a function of slope angle and latitude: results reported in Figure 5 indicate that, for the same latitude and slope exposure (Figure 5a), the seasonal anomaly experiences a stronger oscillation for surfaces with a lower slope angle, while for steep slopes the annual oscillation of the seasonal anomaly is less visible.

Let us first compare the onset and development of slope winds for the same slope on quite different days of the year, namely the two solstices (summer and winter) and one equinox.

The major difference between the different days of the year concerns the duration of the upslope wind component. Moreover, the magnitude of the surface potential temperature perturbation, and consequently the along-slope wind speed, is higher during summertime, as expected. It is interesting to note that, over steep slopes, the almost constant net radiation during nighttime results in

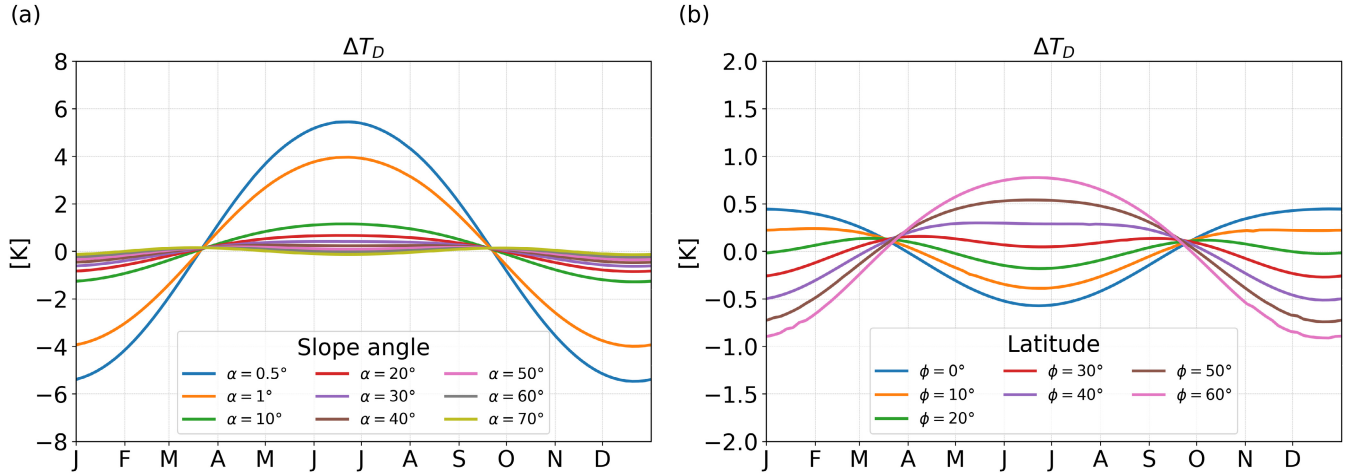

FIGURE 5 Seasonal anomalies as a function of (a) slope angle (for $\phi = 30\circ$) and (b) latitude (for $\alpha = 30\circ$), in the case of south-facing slopes.

a quasi-steady-state flow, with constant potential temperature anomaly and along-slope wind-speed profile. Moreover, the peak in the daily cycle of temperature is slightly delayed with respect to the peaks of net radiation.

A special case is offered by a surface covered with fresh snow. The parameters are the same for the winter solstice case of Figure 6, but with albedo increased to $A = 0.9$. Albedo affects only the evaluation of the seasonal anomaly (Equation 41) and the daily cycle, while the mean annual radiative equilibrium temperature is the same in both cases. Figure 7 shows the daily cycle of net radiation for both the winter solstice (blue lines) and winter solstice with snow cover (turquoise lines).

With the surface covered by snow, the albedo is so high that most of the incoming solar radiation is reflected and over the whole daily cycle the net radiation is always negative, as well as the surface-temperature perturbation. The final result (Figure 7c) is that the wind regime is characterized by a persistent downslope wind, only weakening slightly during the central hours of the day.

The slope angle is one of the factors, along with the temperature gradient of the unperturbed atmosphere (γ_a), discriminating between supercritical and subcritical regimes. Figure 8 compares the slope winds generated over two south-facing slopes in the midlatitudes, with different slope angles, on the summer solstice. For a very gentle slope ($\alpha = 0.5\circ$) and a very stable overlying atmosphere ($\gamma_a = 0.01\ \mathrm{K^{-1}\cdot m}$), the first two harmonics are in the supercritical wind regime, whilst higher-order harmonics are subcritical. In contrast to steep slopes, for gentle slopes the almost constant net radiation during nighttime does not result in a steady state. Instead, the temperature continues to decrease during the night and experiences a minimum shortly before sunrise. Moreover, in the case of a gentle slope, the temperature maximum is delayed by a few hours with respect to the peak of net radiation, with a longer delay for steeper slopes. Nevertheless, the daily excursion experienced by the surface temperature in the case of the gentle slope seems unrealistically high. On the other hand, in realistic situations, it is likely that over nearly flat conditions other processes, not accounted for in the present model (e.g., convection), may be relevant in redistributing the radiative input. Moreover, over the gentler slope, the slope wind layer is deeper than for larger angles, which is likely due to seasonal anomalies and the associated Prandtl-like steady state. In fact, for slope angles approaching zero, the length scale (Equation 10) approaches infinity, resulting in an ideally infinitely extended slope-flow layer (e.g., Mo, 2013).

However, slope angles approaching zero deserve a special remark: no along-slope balance between buoyancy and local momentum can be easily established, hence no thermally driven wind can be generated.

The slope orientation determines the timing of the transitions between upslope and downslope wind regimes. Figure 9 shows the daily onset of slope winds for the summer solstice over steep slopes ($\alpha = 30\circ$), oriented in different directions in midlatitudes. The east-facing slope receives direct sunlight earlier in the morning and thus the upslope wind starts blowing earlier, while for a west-facing slope the onset of the upslope flow is delayed until mid-morning and experiences the strongest development in the afternoon.

4 | DISCUSSION AND CONCLUSIONS

An analytical solution extending the model proposed by Zardi and Serafin (2015) to reproduce a more realistic

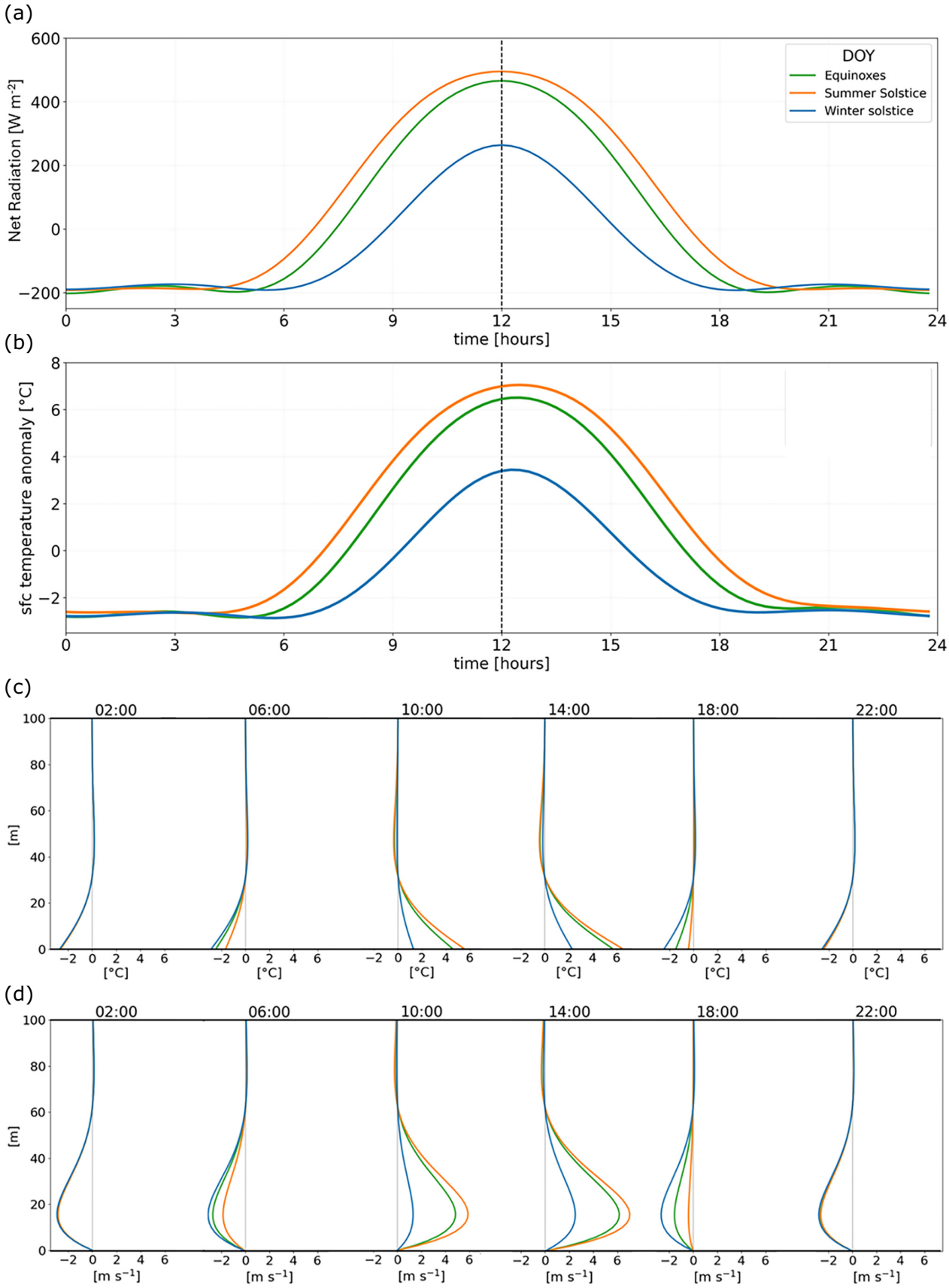

FIGURE 6 (a) Net radiation, (b) surface-temperature perturbation, (c) potential temperature, and (d) along-slope wind profiles for a steep ($\alpha = 30°$) south-facing slope ($\gamma = 0°$), in the midlatitudes (ϕ=45°), at an elevation of 1.5 km for different days of the year.

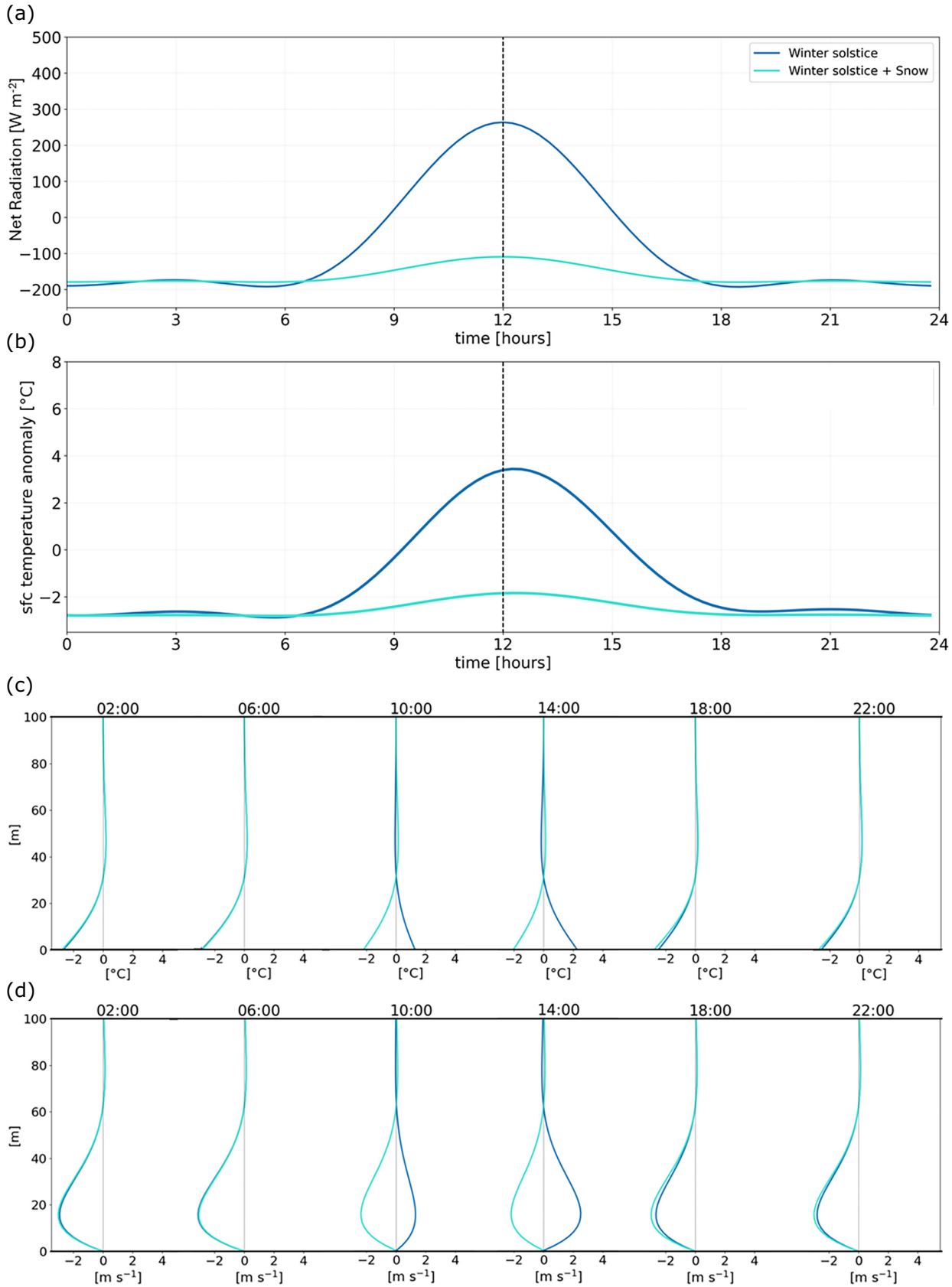

FIGURE 7 (a) Net radiation, (b) surface-temperature anomaly, (c) selected potential temperature, and (d) along-slope wind profiles for a steep ($\alpha = 30°$) south-facing slope ($\gamma = 0°$), in the midlatitudes ($\phi = 45°$) and at an elevation of 1.5 km for the winter solstice. Blue and turquoise represent cases with an absence of snow ($A = 0.2$) and a snow-covered surface ($A = 0.9$), respectively.

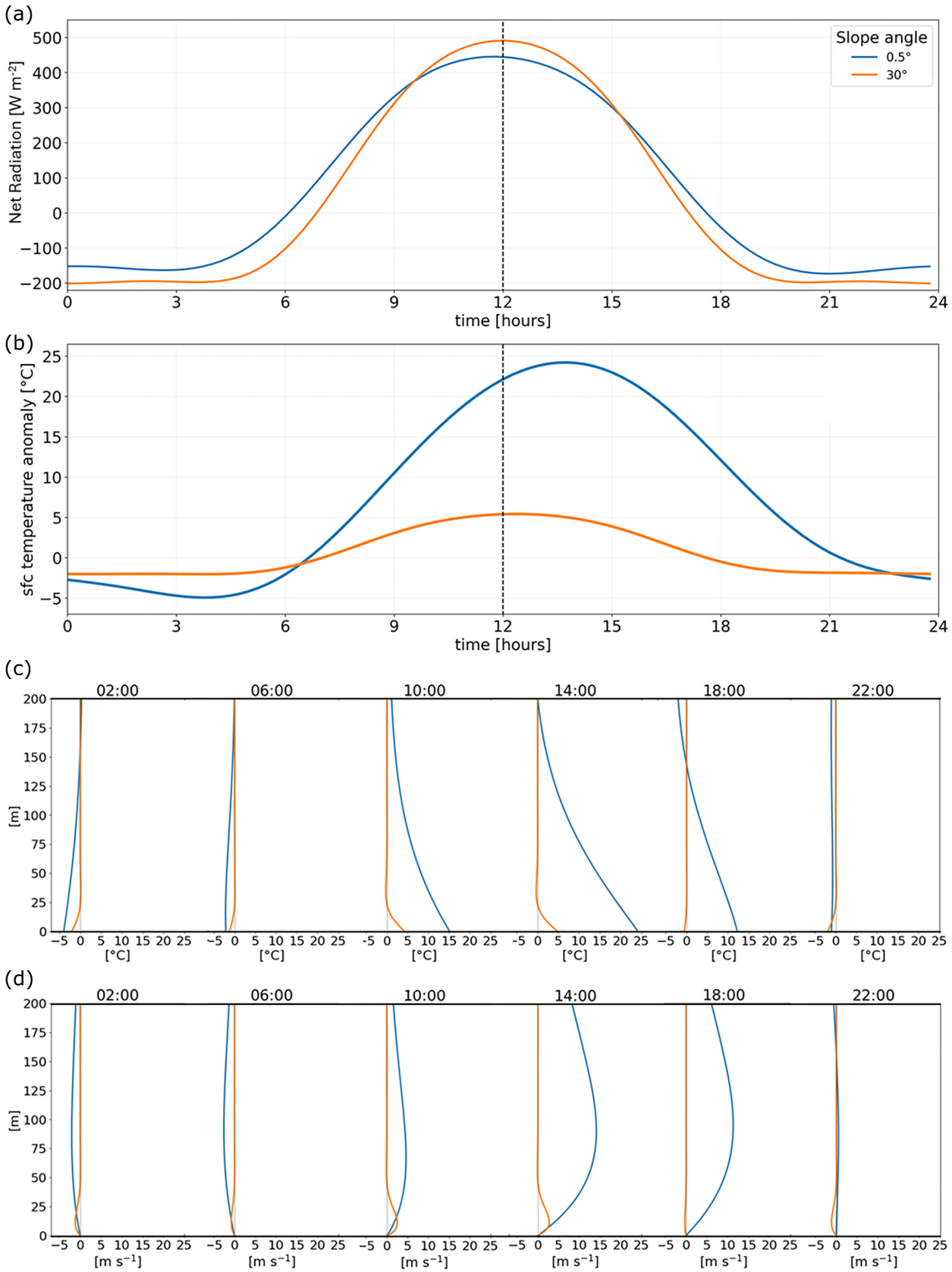

FIGURE 8 (a) Net radiation, (b) surface-temperature perturbation, (c) selected potential temperature, and (d) along-slope wind profiles for the Summer Solstice (DOY = 172) in the midlatitudes (ϕ=45°), for a south-facing slope (γ=0°) at an elevation of 1.5 km. In the case of the $\alpha = 0.5°$ slope, the first two harmonics fall in the supercritical flow regime, while higher-order harmonics fall in the subcritical flow regime.

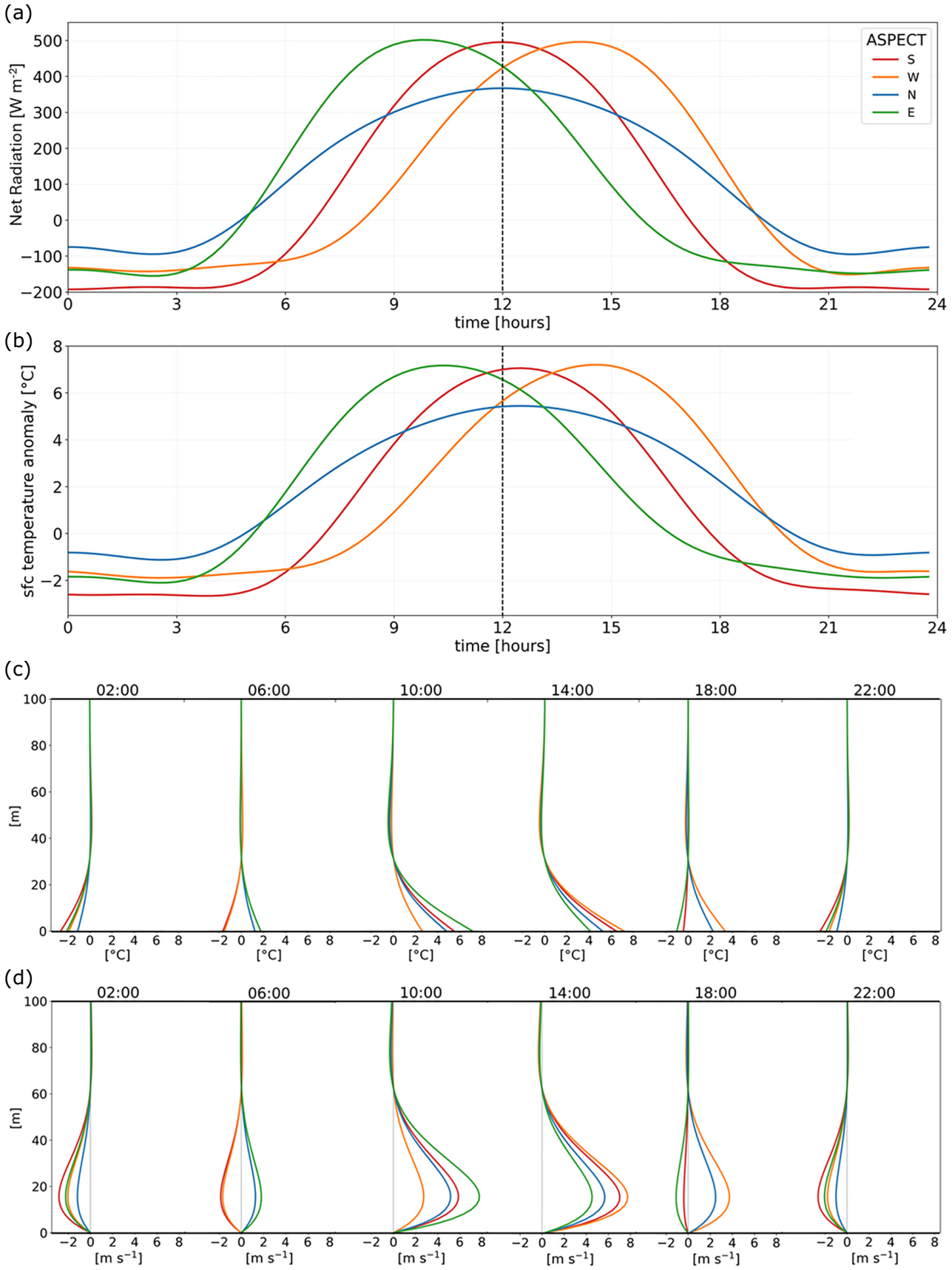

FIGURE 9 (a) Net radiation, (b) surface-temperature perturbation, (c) selected potential temperature, and (d) along-slope wind profiles for the Summer Solstice (DOY = 172) for a steep slope ($\alpha = 30°$), in the midlatitudes ($\phi = 45°$), and at an elevation of 1.5 km, for different orientations of the slope (line colors).

development of daily-periodic slope winds has been proposed. The main extension consists of representing the flow by means of a Fourier series expansion rather than a single harmonic for the surface temperature, with amplitude and phases derived from the SEB. The latter is evaluated by means of the analytical daily-periodic estimate of net incoming radiation presented in Part 1. This provides the physical constraints to derive the daily cycle of surface temperature, which is the ultimate driver of slope winds. The model allows us to show how radiation controls the transition timings between the upslope and downslope wind regimes and their magnitude.

Several conditions and configurations were tested, such as the onset of thermally driven winds on different days of the year for the same slope, the same day of the year for slopes with different slope angles, and finally the same day for slopes oriented in different directions. An interesting feature reproduced by the model is the delay in the temperature maximum with respect to the peak of the radiative forcing. This is more pronounced for gentler slopes, while just barely appreciable for steeper slopes, the response of which appears to be more in phase with the radiative input. Moreover, over steep slopes the almost constant negative net radiation during nighttime results in the formation of a steady-state downslope wind, with constant surface-temperature anomaly and wind speed (as expected from Fedorovich & Shapiro, 2017). On the other hand, over gentler slopes, a minimum in the daily cycle of temperature is observed shortly before sunrise. In addition, the slope orientation plays, as expected, a major role in determining the timing of the transitions between upslope and downslope wind regimes, indicating the fast response of the surface to changes in the radiative forcing. In fact, an east-facing slope will receive sunlight early in the morning, with the build-up of an upslope wind regime lasting until early afternoon, when the slope shades itself from sunlight and the wind regime shifts towards downslope. On the other hand, the upslope wind regime on a west-facing slope does not start until mid-morning, with the diffuse radiation slowly heating up the surface, whereas only around noon does the upslope wind initiate its full development, as soon as the surface receives more direct sunlight. Considering seasonal effects instead, the model shows correctly that on summer days the duration of upslope winds is longer than in winter (apart from snow-covered situations). Also, the surface temperature range, and hence the wind speed, is larger in the warm season.

One of the main limiting factors of the present model consists of the simplified representation of the SEB. Turbulent fluxes associated with thermally driven circulations are assumed to be the only contributors to the sensible heat flux in the SEB, whilst large-scale processes or convection are not taken into account. The resulting surface temperature anomalies are plausible for steep slopes, suggesting that, for these, the above assumptions are acceptable, whilst the high temperature ranges obtained for a gentle slope indicate that other processes not included in the present model might be relevant there. Also, the parameterization of turbulent flux through a k-closure with constant eddy viscosity and heat diffusivity is a rather crude approximation. More sophisticated closures may be tested in further developments of this work. The effects of convection might be accounted for by introducing suitable parameterizations (e.g., counter-gradient), as suggested by numerical simulations (Schumann, 1990). This will be explored in a future development of the present work.

Moreover, accounting for the latent heat flux would require further information about the soil water content and the water vapor content in the atmosphere, for appropriate modeling of soil–atmosphere exchange processes (e.g., evapotranspiration). However, such parameterizations require in turn a suitable model of soil moisture content, which is beyond the scope of the present analysis and may be the subject of future developments.

Another limiting factor is the height of the atmospheric layer affected by the development of the slope wind, which is the same for daytime and nighttime regimes according to the present model. The available observations suggest that the nighttime wind layer is shallower than the daytime one (Whiteman, 2000). A step forward toward improving this aspect could be made by considering different eddy viscosity and diffusivity values for the daytime and nighttime regimes. However, this comes at the expense of more complex analytical solutions. In fact, easy analytical solutions of the equations governing the onset and characteristics of thermally driven circulations can be derived only under the approximation of constant K profiles. A significant improvement in the evaluation of these processes can be attained by means of numerical models, employing different turbulence closures to parameterize the values of K (Zonato *et al.*, 2022). An alternative constitutes assuming constant K profiles with values different for daytime and nighttime, thus accounting for more or less mixing based on the sign of the surface temperature deviation. However, the choice of the K values would be difficult to justify properly without considering the addition of some field data analysis to find optimal values. Furthermore, a rather quick extension of the current model can be achieved by employing linear structures for the K coefficient, an approximation holding at first order (Brun, 2017; Charrondière *et al.*, 2022a, 2022b). Such formulations still allow analytical integration for the derivation of solutions, and at the same time can constitute another step towards a more realistic model.

Despite the above-mentioned limitations, results shown here provide a valuable starting point for the analytical description of realistic thermally driven circulations. In fact, some relevant features connected with slope winds are already well captured at the present stage, and further developments can only reduce the gap toward a comprehensive, analytical model for understanding the physics of the phenomena. This can have multiple benefits, including a better insight into the exchanges of mass, heat, and momentum over complex terrain areas, as well as the transport of species. Further steps towards the improvement of the realism of the model will be fulfilled in future works, especially in the framework of the international research initiative TEAMx—Multi-scale transport and exchange processes in the atmosphere over mountains—programme and experiment (Rotach *et al.*, 2022).

ACKNOWLEDGEMENTS

M. Marchio acknowledges support from the Italian Ministry for Universities and Research (MUR) under the grant "Dipartimenti di Eccellenza (2018-2022)", awarded to the Department of Civil, Environmental and Mechanical Engineering of the University of Trento. S. Farina acknowledges support from the C3A–Center Agriculture Food Environment of the University of Trento and from Consorzio Difesa delle Produzioni Agricole Trento (Co.Di.Pr.A.). D. Zardi acknowledges support from the Italian Ministry for University and Research (MUR) under the project "DECIPHER–Disentangling mechanisms controlling atmospheric transport and mixing processes over mountain areas at different space- and timescales" funded by the scheme "Research Projects of Relevant National Interest–Call 2022 (PNRR2022)", CUPE53D23004450006, Code protocol 2022NEWP4J.

CONFLICT OF INTEREST STATEMENT

The authors declare no conflict of interest.

DATA AVAILABILITY STATEMENT

Data sharing not applicable—no new data generated, or the article describes entirely theoretical research.

ORCID

Mattia Marchio https://orcid.org/0000-0003-4027-8958

REFERENCES

An, N., Hemmati, S. & Cui, Y.-J. (2017) Assessment of the methods for determining net radiation at different time-scales of meteorological variables. *Journal of Rock Mechanics and Geotechnical Engineering*, 9, 239–246. Available from: https://doi.org/10.1016/j.jrmge.2016.10.004

Barry, R.G. (2008) *Mountain weather and climate*. Cambridge: Cambridge University Press.

Brun, C. (2017) Large-Eddy simulation of a katabatic jet along a convexly curved slope: 2. Evidence of Görtler vortices. *Journal of Geophysical Research: Atmospheres*, 122, 5190–5210. Available from: https://doi.org/10.1002/2016JD025416

Carslaw, H. & Jaeger, J. (1959) *Conduction of heat in solids*. Oxford, UK: Oxford Science Publications, Clarendon Press.

Castelli, M., Stöckli, R., Zardi, D., Tetzlaff, A., Wagner, J.E., Belluardo, G. et al. (2014) The HelioMont method for assessing solar irradiance over complex terrain: validation and improvements. *Remote Sensing of Environment*, 152, 603–613. Available from: https://doi.org/10.1016/j.rse.2014.07.018

Charrondière, C., Brun, C., Cohard, J.-M., Sicart, J.-E., Obligado, M., Biron, R. et al. (2022b) Katabatic winds over steep slopes: overview of a field experiment designed to investigate slope-Normal velocity and near-surface turbulence. *Boundary-Layer Meteorology*, 182, 29–54. Available from: https://doi.org/10.1007/s10546-021-00644-y

Charrondière, C., Brun, C., Hopfinger, E.J., Cohard, J.-M. & Sicart, J.-E. (2022a) Mean flow structure of katabatic winds and turbulent mixing properties. *Journal of Fluid Mechanics*, 941, A11. Available from: https://doi.org/10.1017/jfm.2022.281

De Wekker, S.F.J., Kossmann, M., Knievel, J.C., Giovannini, L., Gutmann, E.D. & Zardi, D. (2018) Meteorological applications benefiting from an improved understanding of atmospheric exchange processes over mountains. *Atmosphere*, 9, 371–393. Available from: https://doi.org/10.3390/atmos9100371

Defant, F. (1949) Zur Theorie der Hangwinde, nebst Bemerkungen zur Theorie der berg- und Talwinde. *Archiv für Meteorologie, Geophysik und Bioklimatologie, Serie A*, A1, 421–450.

Farina, S., Marchio, M., Barbano, F., di Sabatino, S. & Zardi, D. (2023) Characterization of the morning transition over the gentle slope of a semi-isolated massif. *Journal of Applied Meteorology and Climatology*, 62, 449–466. Available from: https://doi.org/10.1175/JAMC-D-22-0011.1

Farina, S. & Zardi, D. (2023) Understanding thermally driven slope winds: recent advances and open questions. *Boundary-Layer Meteorology*, 189, 5–52. Available from: https://doi.org/10.1007/s10546-023-00821-1

Fedorovich, E. & Shapiro, A. (2017) Oscillations in Prandtl slope flow started from rest. *Quarterly Journal of the Royal Meteorological Society*, 143, 670–677. Available from: https://doi.org/10.1002/qj.2955

Giovannini, L., Laiti, L., Serafin, S. & Zardi, D. (2017) The thermally driven diurnal wind system of the Adige Valley in the Italian Alps. *Quarterly Journal of the Royal Meteorological Society*, 143, 2389–2402. Available from: https://doi.org/10.1002/qj.3092

Grisogono, B., Jurlina, T., Večenaj, Z. & Güttler, I. (2014) Weakly non-linear Prandtl model for simple slope flows. *Quarterly Journal of the Royal Meteorological Society*, 141, 883–892. Available from: https://doi.org/10.1002/qj.2406

Grisogono, B. & Oerlemans, J. (2001) Katabatic flow: analytic solution for gradually varying eddy diffusivities. *Journal of the Atmospheric Sciences*, 58, 3349–3354. Available from: https://doi.org/10.1175/1520-0469(2001)058<3349:KFASFG>2.0.CO;2

Hatchett, B.J., Kaplan, M.L., Nauslar, N.J., Smith, C.M. & Nelson, K. (2020) Slope winds. In: Manzello, S.L. (Ed.) *Encyclopedia of wildfires and wildland-urban Interface (WUI) fires.*

Cham: Springer. Available from: https://doi.org/10.1007/978-3-319-52090-2&uscore;209

Laiti, L., Andreis, D., Zottele, F., Giovannini, L., Panziera, L., Toller, G. et al. (2014) A solar atlas for the Trentino region in the Alps: quality control of surface radiation data. *Energy Procedia*, 59, 336–343. Available from: https://doi.org/10.1016/j.egypro.2014.10.386

Laiti, L., Giovannini, L., Zardi, D., Belluardo, G. & Moser, D. (2018) Estimating hourly beam and diffuse solar radiation in an alpine valley: a critical assessment of decomposition models. *Atmosphere*, 9, 117–136. Available from: https://doi.org/10.3390/atmos9040117

Mahrt, L. & Larsen, S. (1990) Relation of slope winds to the ambient flow over gentle terrain. *Boundary-Layer Meteorology*, 53, 93–102. Available from: https://doi.org/10.1007/BF00122465

Marchio, M., Farina, S. & Zardi, D. (2024) An analytical model for daily-periodic slope winds. Part 1. Surface radiation budget. *Quarterly Journal of the Royal Meteorological Society*, 150(764), 3911–3924.

Maykut, G.A. & Church, P.E. (1973) Radiation climate of Barrow Alaska, 1962-1966. *Journal of Applied Meteorology and Climatology*, 12, 620–628. Available from: https://doi.org/10.1007/BF00866433

Mo, R. (2013) On adding thermodynamic damping mechanisms to refine two classical models of katabatic winds. *Journal of the Atmospheric Sciences*, 70, 2325–2334. Available from: https://doi.org/10.1175/JAS-D-12-0256.1

Prandtl, L. (1942) *Führer durch die Strömungslehre, chapter 5*. Vieweg und Sohn: Braunschweig, Germany.

Rotach, M.W., Serafin, S., Ward, H.C., Arpagaus, M., Colfescu, I., Cuxart, J. et al. (2022) A collaborative effort to better understand, measure, and model atmospheric exchange processes over mountains. *Bulletin of the American Meteorological Society*, 103, E1282–E1295. Available from: https://doi.org/10.1175/BAMS-D-21-0232.1

Schumann, U. (1990) Large-eddy simulation of the up-slope boundary layer. *Quarterly Journal of the Royal Meteorological Society*, 116, 637–670. Available from: https://doi.org/10.1002/qj.49711649307

Serafin, S., Adler, B., Cuxart, J., De Wekker, S.F.J., Gohm, A., Grisogono, B. et al. (2018) Exchange processes in the atmospheric boundary layer over mountainous terrain. *Atmosphere*, 9, 102–133. Available from: https://doi.org/10.3390/atmos9030102

Stiperski, I., Kavčič, I., Grisogono, B. & Durran, D.R. (2007) Including Coriolis effects in the Prandtl model for katabatic flow. *Quarterly Journal of the Royal Meteorological Society*, 133, 101–106. Available from: https://doi.org/10.1002/qj.19

Van Wijk, W.R. & Scholte Ubing, D.W. (1963) In: Van Wijk, W.R. (Ed.) *Physics of plant environment*. Amsterdam, Netherlands: North-Holland Publishing Company.

Whiteman, C.D. (2000) *Mountain meteorology: fundamentals and applications*. Oxford: Oxford University Press.

Zammett, R.J. & Fowler, A.C. (2007) Katabatic winds on ice sheets: a refinement of the Prandtl model. *Journal of the Atmospheric Sciences*, 64, 2707–2716. Available from: https://doi.org/10.1175/JAS3960.1

Zardi, D. & Serafin, S. (2015) An analytic solution for time-periodic thermally driven slope flows. *Quarterly Journal of the Royal Meteorological Society*, 141, 1968–1974. Available from: https://doi.org/10.1002/qj.2485

Zardi, D. & Whiteman, C.D. (2013) Diurnal mountain wind systems. In: Chow, F., De Wekker, S. & Snyder, B. (Eds.) *Mountain weather research and forecasting*. Berlin, Germany: Springer Atmospheric Sciences. Available from: https://doi.org/10.1007/978-94-007-4098-3&uscore;2

Zonato, A., Martilli, A., Jimenez, P.A., Dudhia, J., Zardi, D. & Giovannini, L. (2022) A new K–ϵ turbulence parameterization for mesoscale meteorological models. *Monthly Weather Review*, 150, 2157–2174. Available from: https://doi.org/10.1175/MWR-D-21-0299.1

How to cite this article: Marchio, M., Farina, S. & Zardi, D. (2024) An analytical model for daily-periodic slope winds. Part 2: Solutions. *Quarterly Journal of the Royal Meteorological Society*, 150(764), 3925–3941. Available from: https://doi.org/10.1002/qj.4787